Promotion effect of cobalt doping on microwave-initiated plastic deconstruction for hydrogen production over iron catalysts

Wentao Li [a,b], Kezhen Qian [a,b,*], Zixu Yang [c], Xiaoxu Ding [c], Wenmin Tian [a,b], Dezhen Chen [a,b]

[a] School of Mechanical and Energy Engineering, Tongji University, Shanghai 200092, China
[b] Shanghai Engineering Research Center of Multi-source Solid Wastes Co-processing and Energy Utilization, Shanghai 200092, China
[c] State Key Laboratory of Chemical Engineering, School of Chemical Engineering, East China University of Science and Technology, Shanghai 200237, China

ARTICLE INFO

ABSTRACT

Microwave-initiated deconstruction of plastic into hydrogen and high-value carbons is an attractive upcycling technology. However, the interplay between microwave field and catalyst material and the reaction mechanism were not fully understood. In this study, Co doping Fe-Al catalysts were synthesized for hydrogen production from LDPE using microwave and conventional heating. The Fe1Co1Al2 catalyst yielded hydrogen at 61.39 mmol/g$_{plastic}$ under microwave, which was almost two times higher than conventional heating. Characterization indicated Co doped spinel iron catalyst under microwave rapidly transformed into the highly active FeCo alloy for plastic dehydrogenation. The microwave field was responsible for the rapid formation of FeCo, as it enhanced the charge transfer from H to Fe. The Co doping also inhibited the formation of Fe$_3$C during plastic deconstruction, which changed the carbon diffusion pathway and promoted the formation of nanotubes and hydrogen production.

1. Introduction

The soaring production of single-use plastics creates a huge amount of non-degradable waste that dramatically threatens the environment. Until 2017, the generation of plastic waste totaled 7 billion tons. Among them, only 10% were recycled, 14% were incinerated, and the remaining 76% were discarded in landfills or the natural environment [1]. Upcycling plastics into fuels and valuable chemicals will help to establish a circular economy.

Many routes have been employed to upcycle plastic, including solvent-based recycling, hydrogenolysis, pyrolysis, and gasification. Meanwhile, the plastics can also be upcycled into hydrogen and carbon nanomaterials via catalytical decomposing under high temperatures. In this process, the polymer chain of waste plastics is firstly pyrolyzed into short-chain hydrocarbons. The hydrocarbons are then fed to a conventionally heated catalytic reformer for hydrogen evolution and CNTs growth over supported metal catalysts (e.g., Ni and Fe). The hydrogen yield and carbon nanomaterial qualities have been optimized by adjusting the catalyst properties (e.g., chemical composition, particle size, and morphology) and operational parameters, such as temperature, steam/plastic ratio, and feed rate [2–5]. Yao et al. [6] reported a higher H$_2$ yield over Fe/γ-Al$_2$O$_3$ (22.9 mmol H$_2$/g$_{plastic}$) than Ni/α-Al$_2$O$_3$ (18.0

mmol H$_2$/g$_{plastic}$) in a two-stage pyrolysis-catalysis of real-world waste plastics. The different catalytic performance was attributed to the larger metal particle size of the Ni/α-Al$_2$O$_3$. Contrarily, Liu et al. [7] found that catalysts with larger metal particle size were more effective in hydrogen production from catalytic gasification of polypropylene (Fe/SiO$_2$-L (25.60 mmol H$_2$/g$_{plastic}$) > Ni/SiO$_2$-L (22.60 mmol H$_2$/g$_{plastic}$) > Ni/SiO$_2$-S (18.10 mmol H$_2$/g$_{plastic}$) > Fe/SiO$_2$-S (15.40 mmol H$_2$/g$_{plastic}$), where L and S refer to catalysts with large or small metal particle size). Nonetheless, the controversial findings on the effect of metal particle size can be related to the interference of different metal types, the textural properties of support, and metal-support interaction, which were not adequately ruled out in these aforementioned studies. The essential role of metal-support interaction was highlighted in a study by Yao et al., who argued that an appropriate metal-support interaction was advantageous for the dispersion and immobilization of metal nanoparticles, which were beneficial for both H$_2$ production and the growth of CNTs [8].

The thermal catalytic decomposition of plastic typically has a moderate hydrogen yield at 20–40 mmol H$_2$/g$_{plastic}$. Jie et al. [9] opened a high-efficient route (> 40 mmol H$_2$/g$_{plastic}$) for H$_2$ production of plastic using microwave-initiated catalysis decomposition. Compared with a series of catalysts, Fe-based metal oxide catalysts are found to be the

most effective catalyst for microwave-initiated catalytic decomposition of polyolefins for H_2 and CNTs production. The good performance of Fe-based metal oxides can be attributed to their excellent microwave adsorption ability, resulting in thermal effect-selective heating. Besides, Fe-based metal oxides have high activity in breaking C-C and C-H bonds and high efficiency in catalyzing CNT growth [10].

Moreover, the non-thermal effect of microwaves may also play an essential role during hydrocarbon conversion, which can reduce activation energy and reaction temperature [9,11]. For example, microwave-initiated propane dehydrogenation (PDH) achieved a superior catalytic performance (conversion: 16%, propene selectivity: 80%) at 450 °C, which is much lower than the reaction temperature in the conventional process [12]. When microwave fields are applied, molecules are easily polarized on the catalyst surface. On the other hand, microwave enhances the stabilization of the transition state of polarized intermediates, resulting in a decrease in activation energy [13]. Examples of increased selectivity, in which parallel competing reactions (e.g., C-C bond cleavage vs. C-H bond cleavage) during catalytic cracking of liquid hydrocarbons and waste polyolefins can be altered under the action of microwave irradiation have also been observed [9,14]. In addition, microwaves can only interact with polar molecules; therefore, the gaseous medium cannot be heated in the most catalytic cracking reaction system. This can significantly reduce the chances of homogeneous gas-phase reactions [15]. These studies not only highlighted the role of microwave irradiation in tuning reaction pathways but also the benefit of selective microwave heating in boosting product desorption and diffusion, as well as suppressing side reactions in the gaseous phase. Although the promotional effects of microwave irradiation on catalytic performance have been extensively discussed in the literature, the intrinsic role of microwaves on the active sites of heterogeneous catalysts and reaction mechanisms is scarcely discussed and poorly understood [16].

Bimetallic or trimetallic alloy catalysts have been developed to further improve the H_2 yield and the quality of CNTs from waste polyolefins [17–19]. The alloyed metal induced both structural and electronic changes to the active metal, resulting in improved metal dispersion, resistance toward sintering, and adsorption properties. More importantly, the metal catalysts' electromagnetic absorbing properties are also altered due to the change in chemical composition [20–22]. Given that cobalt has shown promising performance in improving the H_2 yield from the dehydrogenation reactions of light hydrocarbons (e.g., methane, ethylene, and acetylene) [23–25]. In this contribution, we have modified the Fe-Al spinel catalysts with Co. The main purpose of the present study was to elucidate (i) how catalyst composition changes under microwave-irradiated catalytic dehydrogenation conditions; (ii) the consequences of such changes on microwave heating, catalytic activity, and product selectivity. In contrast to previous studies mainly dealing with the effect of microwave irradiation on catalytic performance, we focus on structural evolution and the structure-activity relationship of catalysts under a microwave field. Specifically, we focused on investigating (1) The effects of Co doping on the structure evolution and microwave absorbing ability of Fe-Co-Al catalyst prepared by SCS, (2) The structure evolution of Fe-Co-Al catalyst under microwave induced plastic decomposition to hydrogen and carbon nanotube growth, (3) The effect of microwave electric field on improving Fe-Co-Al catalyst activity compared with conventional thermo-catalytic plastic for hydrogen production. These findings provide valuable insights into the novel microwave methods for hydrogen production utilizing waste plastics.

2. Experimental section

2.1. Chemical and materials

Citric acid ($C_6H_8O_7 \cdot H_2O$, 99.8%), iron nitrate nonahydrate (Fe(NO_3)$_3 \cdot 9$ H_2O, 99.0%), cobalt nitrate hexahydrate (Co(NO_3)$_2 \cdot 6$ H_2O, 99.0%), manganese nitrate tetrahydrate (Mn(NO_3)$_2 \cdot 4$ H_2O, 98%) and aluminum nitrate nonahydrate (Al(NO_3)$_3 \cdot 9$ H_2O, 99.0%), ethanol (C_2H_5OH, 99.7%), ammonia solution($NH_3 \cdot H_2O$, AR) were purchased from Shanghai Aladdin Biochemical Technology Co., Ltd. The low density polyethylene (LDPE) powder and high density polyethylene (HDPE) powder were obtained from Sinopec Beijing Yanshan Petrochemical Co., Ltd. All chemicals received were used without any further treatment.

2.2. Preparation of catalysts

All catalysts were prepared by solution combustion method (SCS). In a typical preparation of Co-doped Fe-Al catalysts, Fe(NO_3)$_3 \cdot 9$ H_2O, $C_6H_8O_7 \cdot H_2O$, and Al(NO_3)$_3 \cdot 9$ H_2O were dissolved in 100 mL deionized water with molar ratios of 1:2:2. Then, Co(NO_3)$_2 \cdot 6$ H_2O in accordance with the final catalyst composition requirements was added dropwise to the mixture solution and was stirred continuously. At the same time, $NH_3 \cdot H_2O$ was added to maintain the solution's PH at 7. After homogenization, the mixture was heated and stirred at 90 °C in the water bath till it transformed into a gel. The gel was then dried overnight in a vacuum oven. The dried gel was added some ethanol and heated in a muffle furnace at 400 °C to produce a fluffy powder. The resulting powders were hand-crushed with an agate mortar, which were designated as Fe-Co-Al catalysts. Additionally, catalysts of Fe1Co1 and Fe1Mn1 were prepared with a 1:1 molar metal ratio by SCS. The iron oxide was prepared without adding Al(NO_3)$_3 \cdot 9$ H_2O and Co(NO_3)$_2 \cdot 6$ H_2O.

2.3. Characterizations

The crystal phases of the sample were determined by X-ray diffraction (XRD) using a Bruker D8 Advance diffractometer (Cu-Kα, k = 1.5418 Å, 10–80°). Scherrer's equation ($D = \frac{0.89\lambda}{\Delta \cos\theta}$) was used to calculate the average crystallite size of fresh catalysts from the FWHM of main crystalline facets at (220), (311): D is the crystal size, and λ, Δ, and θ stand for the wavelength of the X-rays, the FWHM of the diffraction peak, and the angle of the corresponding peak. Raman spectroscopy was utilized to examine the fresh catalysts by scanning between 50 cm^{-1} and 1200 cm^{-1} (LabRAM HR 800 Evolution, France) with an excitation wavelength of 514 nm. The Fe Mossbauer spectra were recorded with a WissEl/MSPCA spectrometer at room temperature and constant transmission mode using ^{57}Co source. H_2 temperature-programmed reduction (H_2-TPR) was set in a fixed reactor equipped with a thermal conductivity detector (TCD) under a 50 mL/min flow rate of 10% H_2/He. Before reduction, the catalysts were dried with high-purity helium (He) at 400 °C for one hour to remove water and other impurities. After cooling to room temperature under He purging, 0.05 g of fresh samples were reduced in an oven-controlled quartz reactor in the temperature range of 30–900 °C with a rate of 10 °C/min. The structures and morphology of the fresh and spent catalysts were checked by scanning electron microscopy (SEM, Jem-2100 F Jeol) equipped with an energy-dispersive X-ray accessory (EDS) and a high-resolution transmission electron microscope (HRTEM, FEI, Tecnai G2 T20). To measure the EM wave performance, complex permeability (ε_r) and dielectric constant (μ_r) were characterized utilizing coaxial methods in a vector network analyzer (N5244A, Agilent, USA) in the range of 2.0–18.0 GHz. The combination of the catalysts and paraffin wax is 1:1 (an inner diameter of 5 mm with an outer diameter of 7 mm under the thickness of 2 mm).

Gas chromatography analyzed the gas products (7820 A, Agilent, USA) with thermal conductivity detector (TCD) and flame ionization detector (FID). The thermal stability of carbon compounds after the reaction was examined by thermogravimetric analysis (TGA). Approximately 10 mg sample was heated from room temperature to 800 °C at a heating rate of 10 °C/min under 50 mL/min air. In addition, Raman spectroscopy (LabRAM HR 800 Evolution, France) was utilized to

examine the degree of graphitization of the deposited carbon by scanning between 800 cm^{-1} and 3200 cm^{-1} with an excitation wavelength of 514 nm.

2.4. Catalytic performance

A microwave reactor and a thermal reactor (Fig. S1) were utilized to evaluate the catalytic performance of different catalysts. Microwave-induced (multi-mode) catalytic reactor system consisted of a 2.45 GHz microwave generator, a gas supply system, a resonance cavity, and a fixed-bed quartz reactor. For each microwave catalytic experiment, 1 g of LDPE or HDPE was mixed with 0.5 g catalyst. The mixture was placed in a quartz tube reactor (10 mm inner diameter and 12 mm outer diameter). The quartz tube was evacuated and then purged with nitrogen before reaction. The catalytic LDPE decomposition was conducted at 700 W microwave power.

The thermal catalytic decomposition of LDPE was evaluated in a two-stage reactor. The catalysts were loaded on quartz cotton in the lower reactor and the LDPE was loaded in the upper reactor. N$_2$ was used to remove air. When the catalyst bed reached 800 °C, the LDPE was heated to 500 °C at 15 °C/min and kept for 15 min.

Thermal catalytic decomposition of LDPE was also carried out over the catalysts that were reduced by 50 mL/min H$_2$. Both the reduction and catalytic reaction were conducted at 800 °C. We also tested impact of H$_2$ reduction temperature with a lower reduction temperature (500 °C). The detailed procedure was similar to the thermal catalytic decomposition of LDPE over a non-reduced catalyst.

The catalytic decomposition of LDPE was also conducted in a mixture mode. In this mode, the catalyst was mixed with LDPE power and loaded in the quartz tube. After the furnace reached 800 °C, the quartz tube was quickly loaded in the furnace. However, very low yield of hydrogen was detected in this mode.

The yield of catalytic H$_2$, H$_2$ efficiency, gas, solid, and oil production was calculated by the equations respectively:

$$\text{Gas yield} = \frac{\text{Mass}_\text{gas}}{\text{Mass}_\text{plastic}} \times 100\% \ (\text{wt.\%}) \tag{1}$$

$$\text{Solid yield} = \frac{\text{Mass}_\text{solid}}{\text{Mass}_\text{plastic}} \times 100\% \ (\text{wt.\%}) \tag{2}$$

$$\text{Oil yield} = 100\% - \text{Gas yield} - \text{Solid yield} \tag{3}$$

$$H_2 \text{ efficiency} = \frac{\text{Total Mass of } H_2 \text{ in gas product}}{\text{Theoretical Mass of } H_2 \text{ yield}} \times 100\% \tag{4}$$

$$H_2 \text{ yield} = \frac{\text{Mass of } H_2 \text{ produced}}{\text{Mass}_\text{plastic}} \times 100\% \tag{5}$$

2.5. DFT calculations

Details of DFT calculations are given in the Supporting Information.

3. Results and discussion

3.1. Characterization of the fresh catalysts

Fig. 1 shows the XRD patterns and Raman spectra of the fresh Fe-Co-Al catalysts. It is clear that the Fe1Al2 catalyst exhibits only the Fe-Al spinel phase (JCPDS,86−2320). No peaks for crystalline alumina were observed, indicating that Al species existed in the form of Fe-Al spinel or amorphous alumina, which is in close agreement with the literature report on the Fe-Al catalyst prepared using the SCS method [26,27]. Fe-Co-Al catalysts almost exhibit the same diffraction patterns as the Fe1Al2 sample. With increasing Co amount, the overall diffraction peaks of Fe-Co-Al catalysts slightly shift to the higher 2θ angles with increased peak intensities (36.22°−36.66°) (Fig. 1b), meaning that the presence of Co results in a lattice distortion and decrease in crystallinity. Such lattice distortion is mainly induced by the mismatch of ionic radius of Co^{2+} and Fe^{2+} (Fe^{2+} = 0.83 Å, Co^{2+} = 0.82 Å) when some Co atoms substitute the Fe atoms located at tetrahedral sites of FeAl$_2$O$_4$ spinel [28,29]. The average crystal size estimated using Scherrer's Equation shows an increasing trend upon increasing the Co amount (Table S3). On the other hand, the diffraction peaks of the CoAl$_2$O$_4$ spinel are very close to those of the FeAl$_2$O$_4$ spinel, making it difficult to distinguish the features of these two spinel phases from their diffraction patterns. Therefore, the XRD patterns reveal that the fresh Fe-Co-Al catalysts are mixed metal oxides containing FeAl$_2$O$_4$ and CoAl$_2$O$_4$ spinel aluminates.

The bulk structure of the fresh Fe-Co-Al catalysts was further analyzed using Raman spectroscopy. As seen in Fig. 1a, all catalysts exhibit an intense Raman band at around 740 cm^{-1}, which was attributed to the A$_{1g}$ vibration mode of FeAl$_2$O$_4$ spinel [30,31]. For Fe1Co0.3Al2 and Fe1Co1Al2, the bands at around 561 cm^{-1} and 689 cm^{-1} could be attributed to the T$_{2g}$ and A$_{1g}$ modes of CoFe$_2$O$_4$ spinel ferrite [32,33], suggesting the formation of spinel ferrites and enrichment of Co species on the catalyst surface as the Co doping amount increases.

Given that iron is considered the active metal species in microwave catalytic reactions and MES is a very sensitive technique for characterizing ferrous materials, we further performed MES at room temperature to identify the structural, magnetic, and chemical information of Fe
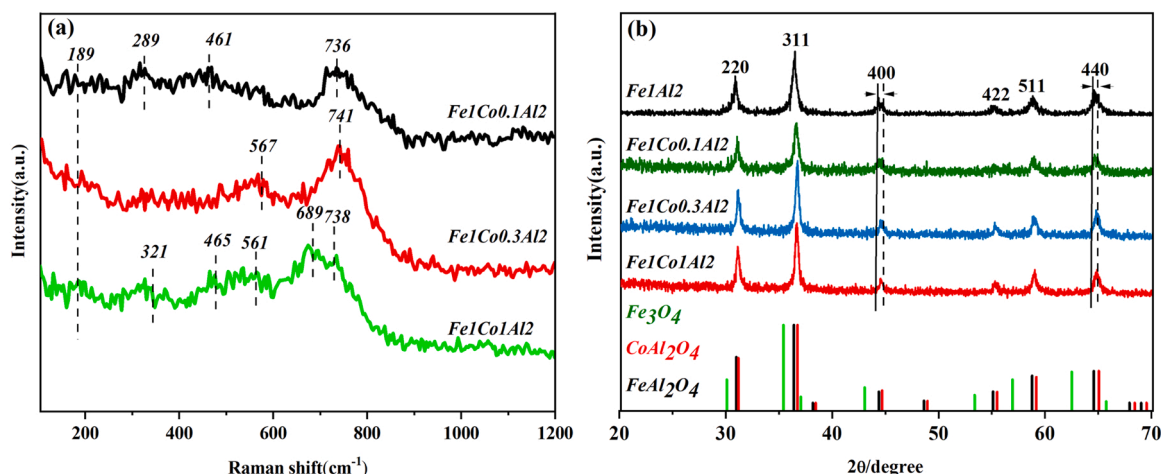

Fig. 1. (a) Raman spectra and (b) XRD patterns of the fresh catalysts.

atoms in fresh catalysts. Fig. 2 displays the ^{57}Fe MES spectra and the deconvoluted subspectra of all catalyst samples generated by curve-fitting, and the fitted hyperfine parameters are shown in Table 1. All catalyst samples contain mostly Fe^{2+} and Fe^{3+} super-magnetic ions, whose presence is indicative of fine iron oxide particles (less than 5 nm). In addition, Fe1Co0.3Al2 and Fe1Co1Al2 contain a certain fraction of sextets with hyperfine fields corresponding to characteristic values of $CoFe_2O_4$ spinel [34]. The presence of Fe^{3+} and Fe^{2+} suggests a disordered cationic distribution in the spinel compound, meaning that some Fe^{3+} ions reside on the O_h sites. The distribution of Fe^{2+} and Fe^{3+} was slightly changed when a small amount of Co was added. With the increase of Co doping amount, the phase transition from superparamagnetic Fe^{3+} to a magnetically ordered $CoFe_2O_4$ phase was observed, manifesting that Co inhibits the Fe-Al interaction.

The micromorphology and surface composition of the fresh catalysts were examined using HR-TEM (Fig. S2 and Fig. S3) and EDS mapping (Fig. S4). All Fe-Co-Al catalysts reveal a compact aggregate of crystals under TEM. The interplanar spacings of 0.468 nm, 0.246 nm, and 0.287 nm were observed, corresponding to the exposure of facets (111), (311), and (220) of Fe-Al spinel, which agree with the XRD patterns.

The EDS elemental mapping reveals that both Fe (cyan) and Al (green) are homogeneously distributed in all samples. The derived overlay image confirms that the Co element is highly dispersed at a low loading amount. However, enrichment of Co element was observed for catalysts with higher loadings. Specifically, the concentrated region of Co overlaps with Fe, indicating that Co interacts with Fe closely in catalysts with high Co dopants. Surface Fe/Co atomic ratios of

Table 1
Fitting parameters of the Mössbauer spectra.

Sample	Components	H_{hf}/kOe	IS (mm/s)	QS (mm/s)	$\Gamma/2$ (mm/s)	Area (%)
Fe1Al2	Doublet 1 (Fe^{3+})	—	0.12	0.88	0.26	43.3
	Doublet 2 (Fe^{2+})	—	0.8	1.54	0.38	56.7
Fe1Co0.1Al2	Doublet 1 (Fe^{3+})	—	0.27	0.89	0.24	38.3
	Doublet 2 (Fe^{2+})	—	0.93	1.59	0.38	61.7
Fe1Co0.3Al2	Doublet 1 (Fe^{3+})	—	0.29	0.85	0.26	65.8
	Doublet 2 (Fe^{2+})	—	0.92	1.56	0.37	29.9
	Sextet ($CoFe_2O_4$)	468.65	0.47	0.26	0.2	4.3
Fe1Co1Al2	Doublet 1 (Fe^{3+})	—	0.31	0.79	0.26	50.9
	Doublet 2 (Fe^{2+})	—	0.91	1.57	0.37	31
	Sextet ($CoFe_2O_4$)	485.86	0.35	0.11	0.66	18.1

Fe1Co0.1Al2, Fe1Co0.3Al2, and Fe1Co1Al2 are measured as 9.82, 2.78, and 0.89, respectively very close to the nominal ones (Table S3).

Based on the results of XRD, MES, HR-TEM, and EDS mapping, it can be concluded that the Co-doped Fe-Al oxides primarily consist of Fe-Al
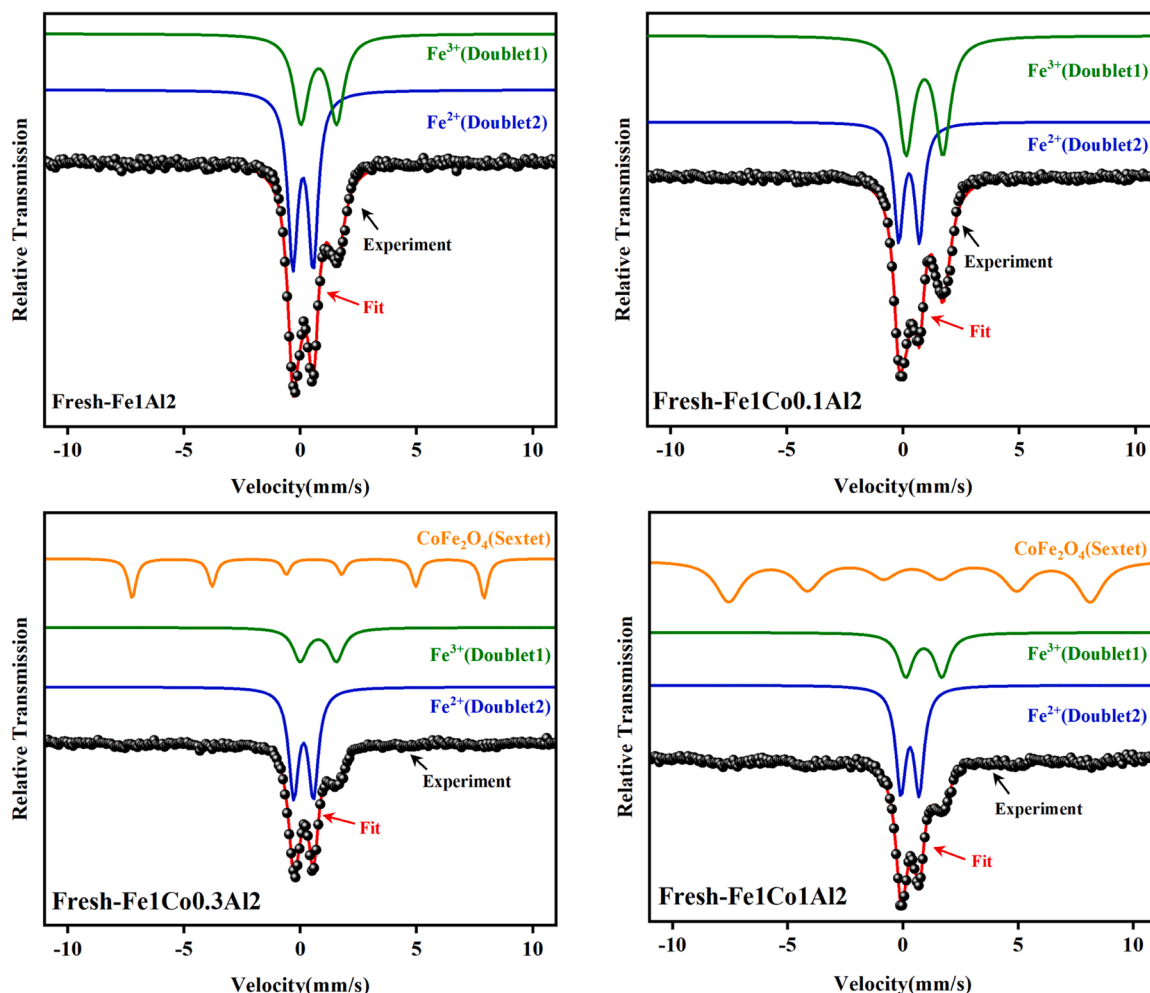
Fig. 2. Mössbauer spectra of the fresh catalysts.

spinel phases with disordered cation distribution. Co can induce the lattice contraction of Fe-Al spinel, as evidenced by shifting diffraction peaks to lower 2θ angles. More importantly, the interaction between Fe and Co was favored as the Co amount increased, resulting in phase transformation from Fe-Al spinel to the $CoFe_2O_4$ spinel phase.

3.2. Characterization of the spent catalysts

The spent catalysts after microwave-initiated catalytic conversion of LDPE were characterized by room-temperature MES and XRD to determine the phase composition. The spectra and curve-fitting parameters are shown in Fig. 3 and Table 2. The spent catalysts show a superposition of two doublets and two sextets, which are characteristics of the supermagnetic and ferromagnetic Fe species, respectively. The hyperfine magnetic field (H_{hf}) values of ca. 343.16 kOe (spent Fe1Co0.1Al2), 367.16 kOe (spent Fe1Co0.3Al2), and 347.1 kOe (spent Fe1Co1Al2) can be attributed to FeCo alloy, according to Stanfield and Delgass [35]. The sextet with a lower H_{hf} value corresponding to the characteristic of the Fe_3C phase was also observed. Fe_3C, created by permeation and diffusion of C atoms through bulk Fe metal has been found to catalyze the growth of carbon nanotubes and nanofibers [36].

Interestingly, the addition of Co definitely decreases the content of Fe_3C from 12.1% to 0, with a sharp increase in FeCo content from 51.7% to 91.4%. Furthermore, the contents of both super magnetic Fe^{2+} and Fe^{3+} show a decreasing trend upon Co addition. This indicates that alloying Fe with Co increases the reducibility while reducing the carburization degree, with the latter being related to the increased carbon diffusion barrier. In metallurgy, alloying Fe with other metals (e. g., Co, Ni, Cr) has been widely used to improve the mechanical and anti-corrosive properties of the metal since the alloyed metal atoms can

Table 2
Fitting parameters of the Mössbauer spectra of the spent Fe1Co1Al2 catalyst (corresponding to Fig. 3).

Sample	Mössbauer spectra	H_{hf}	IS	QS	$\Gamma/2$	Area
	Components	(kOe)	(mm/s)	(mm/s)	(mm/s)	(%)
Spent	Doublet 1 (Fe^{3+})	—	0.2	0.59	0.25	7.7
Fe1Co0.1Al2	Doublet 2 (Fe^{2+})	—	0.92	1.67	0.35	28.5
	Sextet 1(FeCo)	343.16	0.02	0	0.22	51.7
	Sextet 2(Fe_3C)	204.57	0.19	0.09	0.16	12.1
Spent	Doublet 1 (Fe^{3+})	—	0.42	0.98	0.17	3.9
Fe1Co0.3Al2	Doublet 2 (Fe^{2+})	—	0.96	1.64	0.34	10.3
	Sextet 1(FeCo)	367.16	0.03	0	0.23	78.7
	Sextet 2(Fe_3C)	210.6	0.1	0.16	0.15	7.1
Spent	Doublet 1 (Fe^{3+})	—	0.2	0.61	0.17	3.9
Fe1Co1Al2	Doublet 2 (Fe^{2+})	—	0.94	1.68	0.21	4.8
	Sextet 1(FeCo)	347.1	0.03	-0.01	0.22	91.4

reduce carbon solubility and diffusivity [37]. On the other hand, cobalt is more resistant to carburization than iron under carbon-bearing environments [38]. Phase composition determined by MES evidences the reduction and carburization of ferrous precursors into FeCo alloy and Fe_3C initiated by the in situ formed reducing gaseous species (e.g., H_2, CO, C_2H_4) during microwave catalytic decomposition of LDPE.

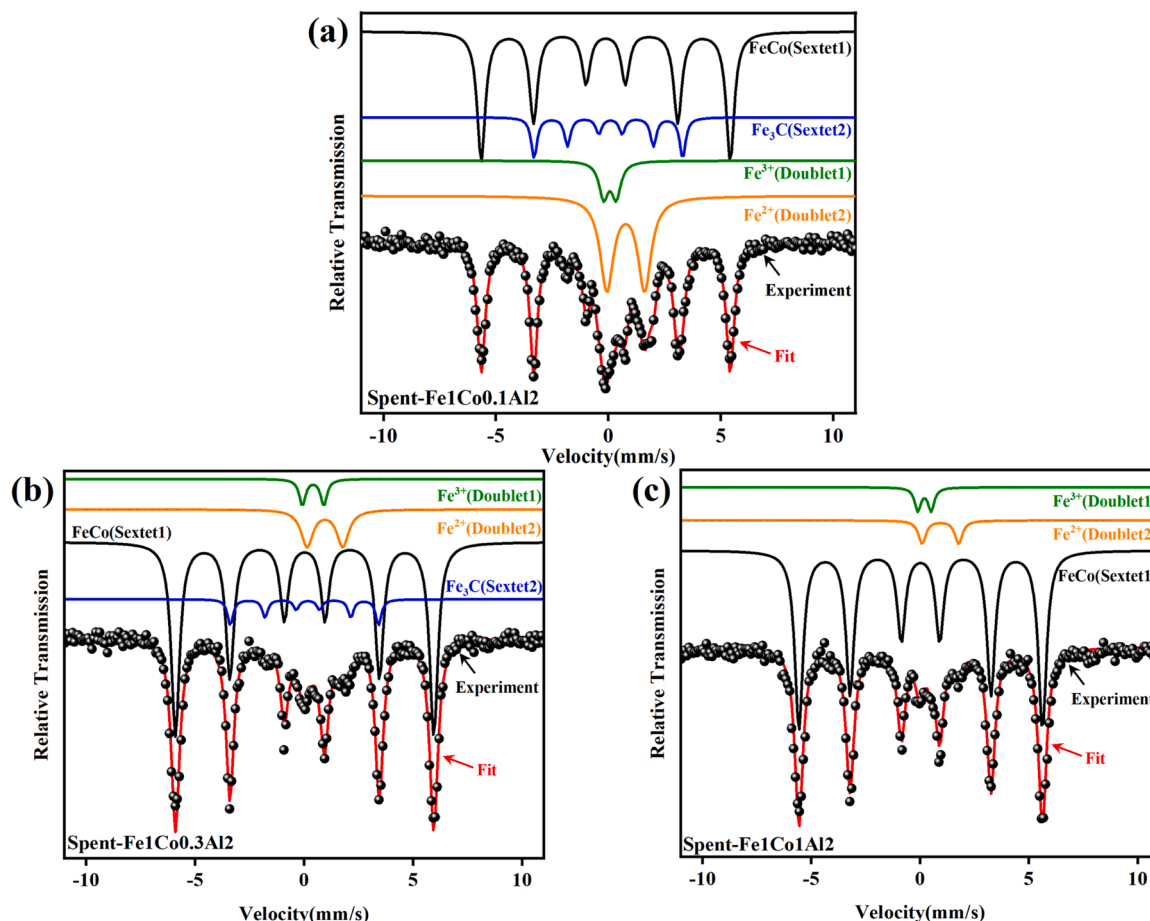The spent Fe-Co-Al catalysts mainly consist of the FeCo alloy phase,

Fig. 3. Mössbauer spectra of the spent Fe-Co-Al catalyst.

as confirmed by the XRD result (Fig. S5), which manifests the reduction from spinel ferrite to metallic iron during the reaction. The rapid dynamic phase change on the Fe1Co1Al2 catalyst during the microwave-initiated catalytic reaction was further investigated by quasi-in situ XRD measurements. As shown in Fig. 4(a), no diffraction peaks of LDPE were observed after 1 min microwave reaction. In the meantime, a sharp diffraction peak corresponding to the plane (110) of FeCo alloy at $2\theta = 44.8°$ appeared, and the intensity of Fe-Al spinel peaks dramatically abated and gradually diminished after 3 min. The absence of the iron carbide phase in the XRD pattern during microwave reaction reconciles the MES result.

Nevertheless, the iron carbide can be amorphous under microwave reaction conditions in this study. These results further highlight the superior reducibility of spinel ferrites under microwave irradiation. For comparison, XRD patterns of Fe1Co1Al2 were collected at various time-on-stream during the thermal reduction in H_2. The prominent diffraction peaks of Fe-Al spinel after 120 min time-on-stream demonstrate that the reduction rate under thermal conditions is significantly slower than that under microwave irradiation (Fig. 4b). The microwave-initiated synthetic method has been widely used for the synthesis of nanomaterials, organics, and metal alloys. In microwave-initiated chemical synthesis, samples are volumetrically heated quickly, allowing uniform nucleation and a shorter crystallization time [39–41]. As for microwave-initiated synthesis of metal nanoparticles, metal precursors are reduced using a microwave-responsive organic solvent (e.g., polyols, resins, hexane), which serves as a reaction medium and reducing agent [42]. Apparently, LDPE does not possess these two properties due to its microwave transparency and nonfluid. The hydrocarbon intermediates from LDPE depolymerization, on the other hand, are readily polarized by microwave, thus creating a localized reaction environment analogous to wet synthesis.

Moreover, the accumulation of carbon deposits enhances the formation of hotspots and triggers the carbothermal reduction of metal oxides under microwave irradiation. This is corroborated by the presence of CO in the gaseous product. From the perspective of catalyst materials, the formation of microwave-induced dipoles on the surface increases the electron migration rate between the catalyst and the adsorption intermediates, resulting in lower activation energy for catalyst reduction.

3.3. Microwave absorbing properties of the catalysts

Microwave absorption performance of the material under an electromagnetic field is intrinsically dependent on its magnetic and dielectric properties, which are typically measured by complex magnetic permeability μ (μ = μ'-jμ''), and complex permittivity ε (ε = ε'-jε''). The real parts, i.e., μ' and ε', represent the magnetic and electric energy storage capability, while the imaginary parts, i.e., μ'' and ε'', refer to the magnetic and electric loss of the material. The loss tangent (tanδ) is usually used to represent the capability of converting electromagnetic energy to other forms of energy, e.g., heat, where tanδ$_m$ (Eq.8) and tanδ$_e$ (Eq.9) are magnetic loss and electric loss tangent, respectively. The Reflection loss (RL) is used to measure the amount of reflected electromagnetic energy due to impedance mismatch, which can be expressed using Eqs. (6), (7), (8), (9), (10), (11) and (12).

$$\varepsilon_r = \varepsilon' - j\varepsilon'' \tag{6}$$

$$\mu_r = \mu' - j\mu'' \tag{7}$$

$$tan\delta_m = \mu''/\mu' \tag{8}$$

$$tan\delta_e = \varepsilon''/\varepsilon' \tag{9}$$

$$Z_0 = \left(\frac{\mu_0}{\varepsilon_0}\right)^{0.5} \tag{10}$$

$$Z_{in} = Z_0\left(\sqrt{\frac{\mu_r}{\varepsilon_r}}\right)\tanh\left[j\left(\frac{2\pi fd}{c}\right)\left(\sqrt{\mu_r \varepsilon_r}\right)\right] \tag{11}$$

$$R_L = 20\log\left(\frac{Z_{in} - Z_0}{Z_{in} + Z_0}\right) \tag{12}$$

Here, Z_0, Z_{in}, f, c, and d are attributed to the impedance in a vacuum, normalized input impedance, microwave frequency; thickness of the absorbing layer; and the velocity of the electromagnetic wave in a vacuum, respectively.

Microwave absorption properties of the Fe-Co-Al catalysts, including magnetic permeability (ε), electric permittivity (ε), loss tangent (δ), and reflection loss (RL) as a function of electromagnetic wave frequency (2–18 GHz) are displayed in Fig. 5. For all Fe-Co-Al catalysts, the value of ε' and ε'' decreased slowly with slight fluctuations as the frequency increases and eventually stabilized at high frequencies, and both values decrease as Co content increases. The decrease in permittivity can be explained as a result of the decrease in Fe^{2+} ions, which are more easily polarized according to the literature survey [43]. Variations of real and imaginary parts of magnetic permeability with electromagnetic frequencies are shown in Fig. 5(b). The μ' and μ'' of the fresh Fe-Co-Al
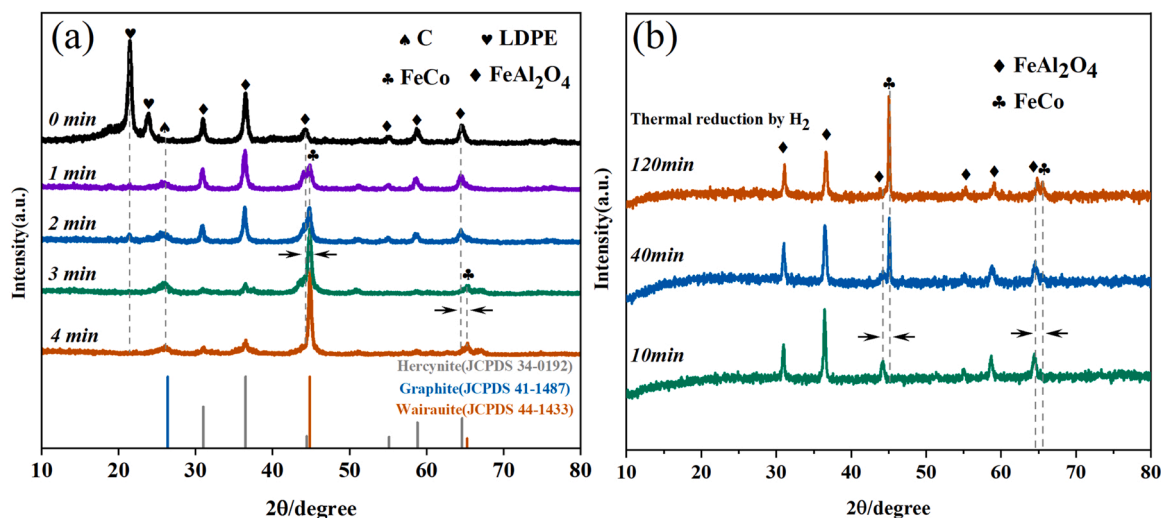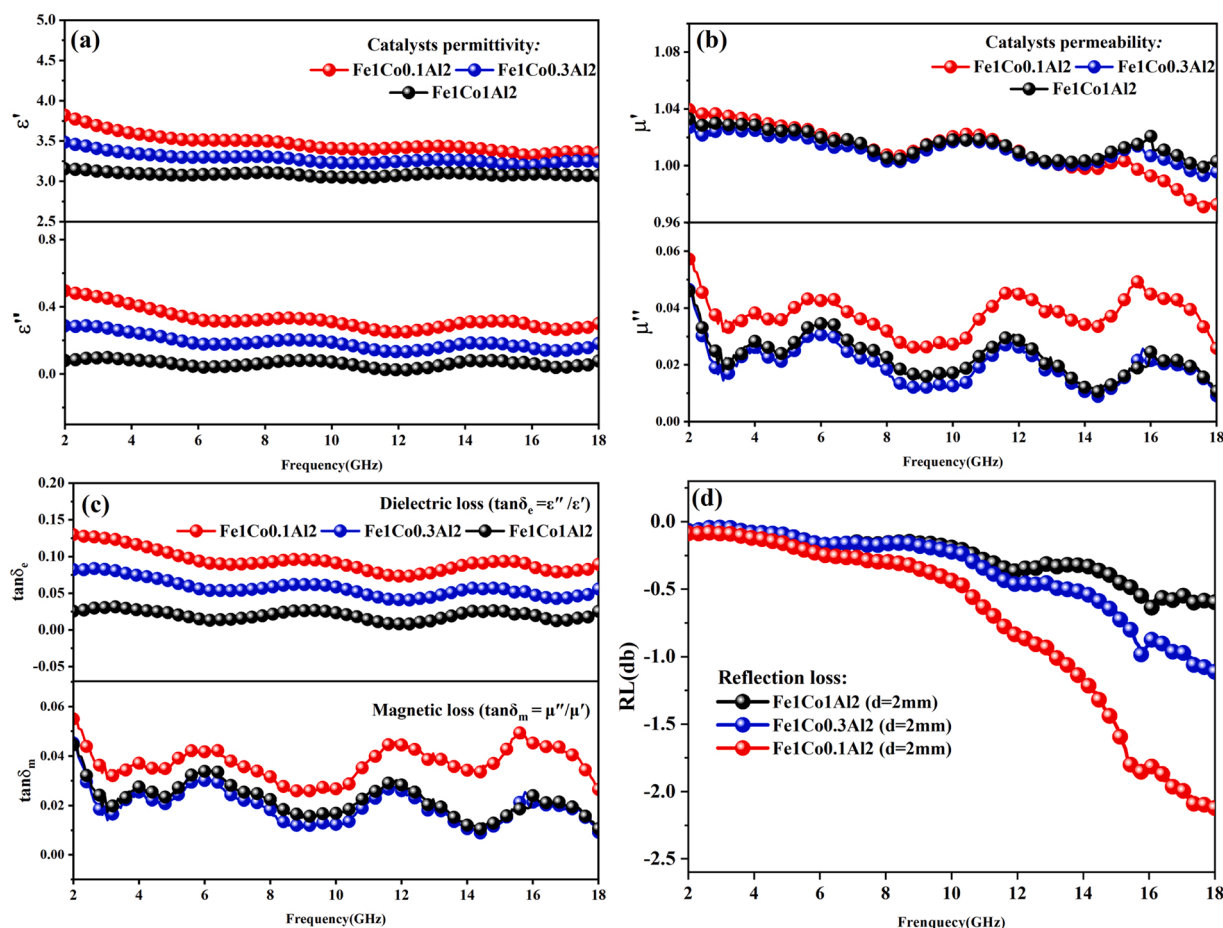

Fig. 4. XRD for (a) mixed samples (plastic and Fe1Co1Al2 catalysts) exposed to microwave irradiation for 0 min, 1 min, 2 min, 3 min, and 4 min after reactions began and (b) Fe1Co1Al2 catalysts reduced by H_2 under a thermal situation (800 °C, 10%H_2/N_2, 50 mL/min).

Fig. 5. Electromagnetic parameters of Fe-Co-Al samples characterized by coaxial method (an inner diameter of 5 mm with an outer diameter of 7 mm under the thickness of 2 mm).

catalysts exhibit modest fluctuations at the tested frequencies, with the former ranging from 0.96 to 1.04 and the latter varying from 0.01 to 0.06. These results show that fresh Fe-Co-Al catalysts are not efficient magnetic lossy materials. Loss tangents of permittivity and permeability also decreased on Co addition and showed almost the same trend as ε' and μ' upon varying frequencies. It is possible that the presence of $CoFe_2O_4$ prevents it from matching the impedance of the Fe-Al spinel [44].

The microwave absorption capacity of a single-layer material under a normalized input impedance can be expressed using reflection loss. A small value of reflection loss indicates strong microwave absorption. As shown in Fig. 5(d), the RL value increases with Co addition, with Fe1Co0.1Al2 having the minimum RL up to − 2 db. Obviously, with the addition of Co-doping, the ability of catalysts' microwave absorption can be effectively reduced, which is consistent with Fig. S6.

3.4. Microwave catalytic performance of the plastic deconstruction

3.4.1. Syngas composition and H_2 yield from microwave-catalysis of plastics

Prior to investigating the performance of Fe-Co-Al catalyst in catalyzing LDPE cracking under microwave irradiation, we examined the catalytic performance of a variety of Fe-based catalysts (Fe_3O_4, Fe1Co1, Fe1Mn1) prepared via the solution combustion method. For comparison, the thermal decomposition behavior of LDPE under microwave irradiation was carried out using SiC as the microwave absorber.

As shown in Figure 6a, H_2, CO, and C_2-C_3 hydrocarbons are the major compounds in the gaseous products of microwave-initiated LDPE decomposition. The H_2 yield obtained from catalytic cracking over Fe-

based catalysts is significantly higher (Fe_3O_4, 25.28 mmol/$g_{plastic}$, Fe1Co1, 35.38 mmol/$g_{plastic}$, Fe1Mn1, 40.18 mmol/$g_{plastic}$) than that obtained from thermal decomposition (SiC, 8.51 mmol/$g_{plastic}$). The CO yield was noticed to vary with different Fe-based catalysts, pointing to the reduction of ferrites by in situ-formed hydrocarbon species released during LDPE cracking. The preliminary catalyst screening proved Fe1Co1Al2 to be the most efficient catalyst for H_2 production from LDPE (H_2 yield of 61.39 mmol/$g_{plastic}$), as compared to other Fe-based bimetallic catalysts. It should also be noted that Fe1Co1Al2 produces almost twice as much H_2 as Fe1Co1. We also tested the microwave decomposition of HDPE with different catalysts. As seen in Fig. S7, catalytic decomposition of HDPE with Co doping iron catalyst had a high hydrogen selectivity (84%) and H_2 yield (53.62 mmol/$g_{plastic}$). Increasing cobalt doping also increased the hydrogen yield.

In comparison to H_2 selectivity and yield of catalytic pyrolysis from reported studies in Table S6, our Fe-Co-Al catalysts exhibit superior selectivity on H_2 and excellent promotion for the H_2 yield in the microwave-initiated pyrolysis of waste plastics. In addition, Al is known to be microwave transparent and mainly serves as a support for active metal components in heterogeneous catalysis. Therefore, we suspect that the high dispersion of Fe species is critical in microwave catalysis, and this inspires us to focus on optimizing the Fe-Al catalyst system for high-purity H_2 production from catalytic cracking of LDPE under microwave irradiation.

Gas/liquid/solid yields, gas composition, H_2 yield, H_2 efficiency, and the temperature recorded during the reaction using Co-doped Fe-Al catalysts were shown in Fig. 6b, c, and d. Due to the addition of Co resulting in an adverse impact on the microwave absorption capacity of the catalysts, as discussed previously, Fe1Co0.1Al2 has a faster heating
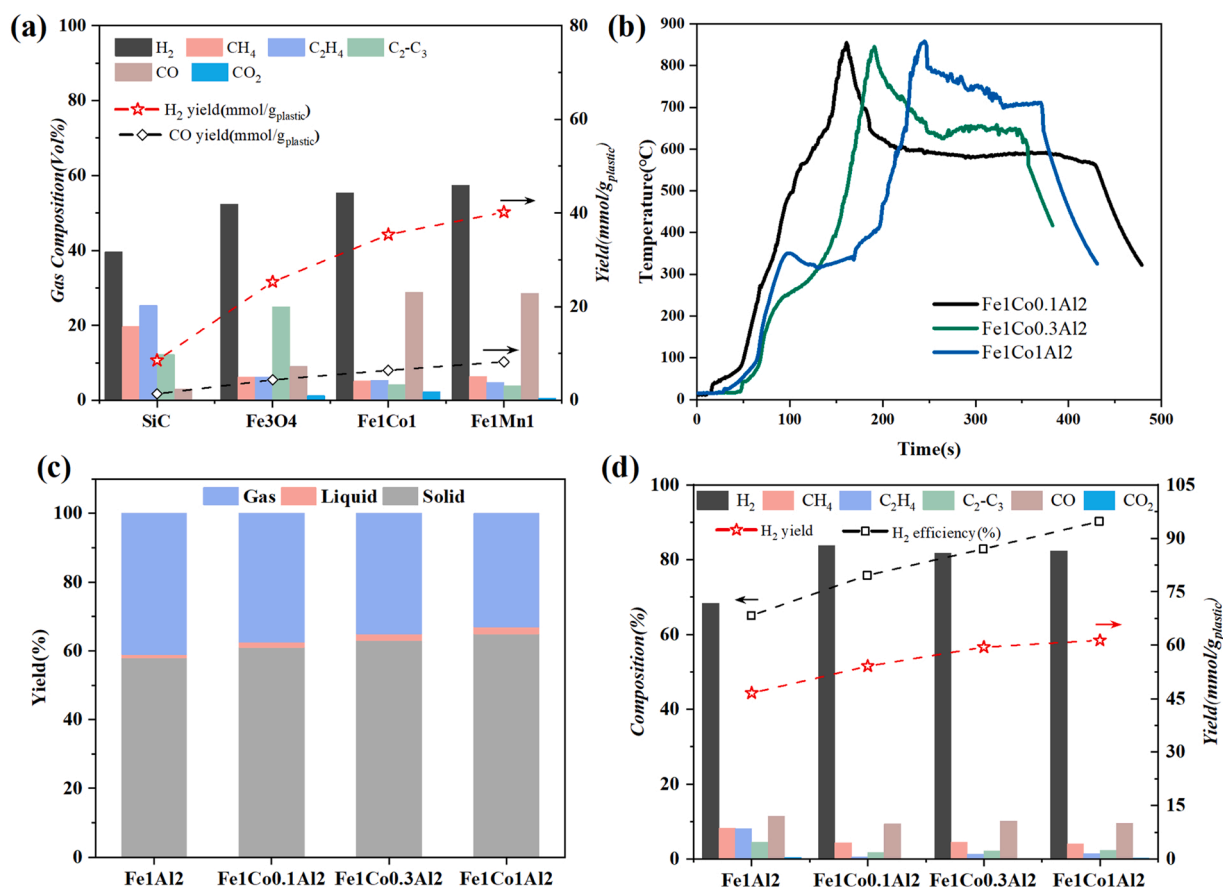
Fig. 6. (a) Microwave experiments using SiC, Fe₃O₄, Fe1Co1, and Fe1Mn1 samples. (b) the temperature recorded by a thermocouple as a function of the time during microwave experiments. (c) Gas/liquid/solid yields of microwave-initiated plastic deconstruction with different Fe-Co-Al catalysts (d) Microwave experiments using Fe-Co-Al catalysts.

rate than others, as shown in Fig. 6b. While the maximum and final stable temperatures are found to be independent of the Co amount. This can be attributed to the generation of carbon nanotubes, which is an efficient microwave absorber, during the reaction. Co-bearing Fe-Al catalysts exhibit higher H_2 yield and H_2 concentration in the gaseous product than nonpromoted Fe1Al2 catalysts. Additionally, the H_2 yield and H_2 efficiency, which is the percentage of hydrogen recovered from LDPE, exhibit a monotonically increasing trend with increasing Co amount. The hydrogen composition of the gas also increased with reaction time (Fig. S7). As the FeCo alloy increased with time (Fig. 4), the increase in hydrogen composition supported the assumption that FeCo alloy is the main active phase.

According to the discussion above, the Fe-Co-Al catalyst undergoes a phase change from Fe-Al spinel to a mixture of FeCo alloy and Fe_3C during microwave-initiated LDPE cracking, with the latter two being active for carbon nanotube growth. Because the amount of liquid product is minimal, the H_2 production rate is linked to the growth of carbon nanotubes during microwave-initiated LDPE cracking. Hence, the promotional effects of Co on H_2 formation and the growth of carbon nanotubes will be discussed later.

3.4.2. Carbon nanomaterials from microwave-catalysis of plastics

Carbon nanotubes can be produced as a valuable solid byproduct via the single-step microwave-initiated catalytic decomposition using LDPE as the feedstock. The micromorphology of the carbon products deposited on the surface of the spent catalysts was investigated using TEM (Fig. 7) and SEM (Fig. 8(a-c)). Filamentous carbons and encapsulated amorphous carbons were clearly observed. A closer look at the TEM images obtained at higher magnification (Fig. 7(d-f)) confirms that these

filamentous carbons are multi-wall carbon nanotubes of various diameters ranging from ca. 6–24 nm. We also noticed a significant difference in the morphological characteristics of carbon nanotubes obtained from different Fe-Co-Al catalyst compositions. Specifically, Fe1Co0.1Al2 exhibits sparsely covered carbon nanotube arrays with long lengths. In contrast, Fe1Co0.3Al2 and Fe1Co1Al2 were covered by a much denser and more entangled filamentous carbon layer. Besides, these two catalysts included more amorphous carbons and encapsulated metal nanoparticles. Interestingly, bamboo-like morphology with thick separating joints was observed in Fe1Co0.1Al2-catalyzed filamentous carbons. It has been reported that CNTs obtained from Fe_3C typically exhibit a bamboo-like morphology due to a slower carbon diffusion rate [45,46]. Both Fe_3C and metallic Fe are found to be active in catalyzing the growth of carbon nanotubes at temperatures above 600 °C. He [47] and his colleagues compared the growth patterns of CNT on Fe_3C and α-Fe. CNT produced with Fe_3C shows a bamboo-like structure, which is commonly designated as a tip-growth mechanism. The authors also observed a slower growth rate over Fe_3C than α-Fe, which was attributed to a slower graphene nucleation rate at step edges of nanoparticles and migration rates of these steps. Of the diameters of carbon nanotubes over all catalysts, Fe1Co0.1Al2 particles could synthesize thinner nanotubes as they have slightly smaller particle size. At the same time, they may also form thicker carbon tubes due to metal accumulation by microwave or the formation of Fe_3C. CNT growth on metal nanoparticles generally follows two mechanisms, depending on the strength of the metal-support interaction: a weak metal-support interaction usually favors a tip-growth mechanism, where the metal nanoparticles are lifted on the tip of the CNT; a strong metal-support interaction anchors the metal nanoparticle firmly, which results in a base-growth mechanism,
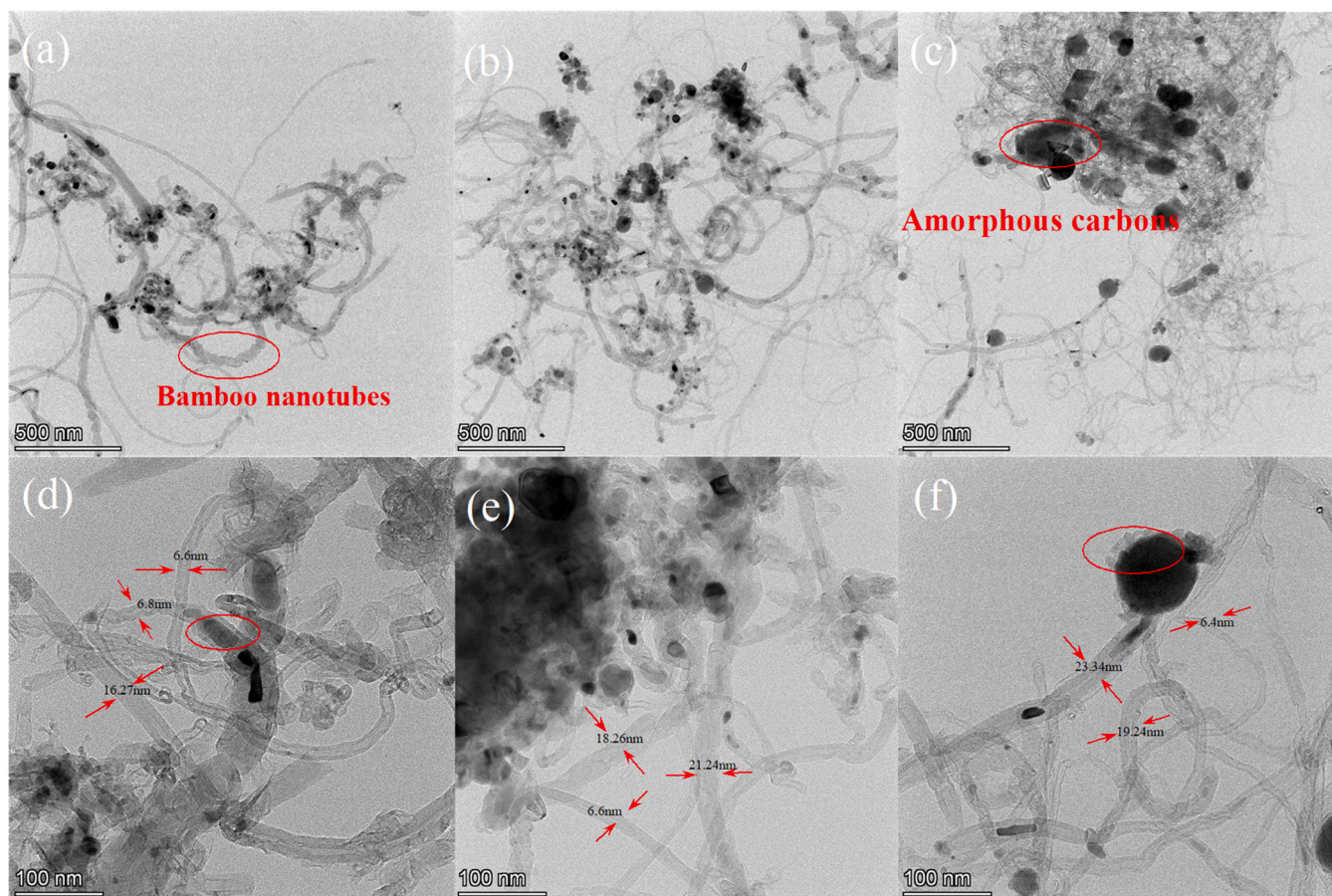
Fig. 7. TEM images of spent (a, d) Fe1Co0.1Al2, (b, e) Fe1Co0.3Al2, and (c, f) Fe1Co1Al2 after microwave catalytic reaction.

where carbons deposit and grow on the surface of metal nanoparticles. As shown in the TEM images, metal nanoparticles can be seen on CNT tips and in the middle of the long fiber, indicating the presence of both growth mechanisms during the reaction. The metal-support interaction was found to be strengthened with increasing Co amount, as evidenced by the upshifting of the reduction peaks in H_2-TPR profiles (Fig. S8).

Raman spectroscopy was performed to evaluate the purity and graphitization of the carbon products obtained from LDPE cracking, and the results are shown in Fig. 8e. Two peaks were observed in Raman spectra at 1340 cm^{-1} (D-band) and 1580 cm^{-1} (G-band), where the G-band is related to the planar motion of ordered sp^2-hybridized carbon, while the D-band is attributed to amorphous carbon, sp^3 disordered structure in carbon materials or sidewall defects in CNTs [48]. The ratio of I_D/I_G, which is an index of graphitization degree, shows an increasing trend towards Co. This indicates that Co can decrease the formation rate of graphite layers on the catalyst surface, resulting in a poor graphitization degree despite an increase in overall carbon yield.

The relative contents of carbon deposits on the catalyst were determined by the TGA experiment in an inert atmosphere, and the results are shown in Fig. 8d. The weight gain at a temperature between 300 and 400 °C was attributed to the oxidation of metallic or carbide Fe [49]. The weight loss starts at about 450 °C, which is attributed to the oxidation of carbon deposits. Since graphite is more stable than amorphous carbon, its oxidation takes at a higher temperature region (550–700 °C) with a slower rate. The inflection point, which corresponds to the maximum weight loss rate on the DTG curve, can be used as a critical point of amorphous and graphite carbon. The temperature of the critical point is then considered as the onsite temperature for the oxidation of graphite carbon [50]. Using this method, the graphite carbon content of the spent catalysts is estimated as 6.34 wt.%, 8.57 wt.

%, and 10.23 wt.% for Fe1Co0.1Al2, Fe1Co0.3Al2, and Fe1Co1Al2 catalysts, respectively. According to TGA and Raman results, Fe1Co1Al2 produced a higher yield of carbon nanotubes, whereas Fe1Co0.1Al2 produced carbon nanotubes with higher crystallinity and order of the walls. This indicated that the plastic decomposition over Fe1Co1Al2 alloy might have a different pathway. Fe_3C in Fe1Co0.1Al2 is beneficial to improve the purity of carbon nanotubes, while FeCo in Fe1Co1Al2 has higher carbon and hydrogen production rates.

In summary, we conclude that Co doping slightly lowered the quality of carbon nanotubes or the degree of graphitization of carbon. At the same time, Co doping hindered the presence of Fe_3C, which changed the carbon diffusion route and promoted the formation of carbon nanotubes and hydrogen production activity.

3.5. Thermal catalytic performance of the plastic deconstruction

We also compared the catalytic decomposition of LDPE using a two-step thermal pyrolysis-catalysis process. The LDPE was firstly pyrolyzed at 500 °C under an N_2 flow rate of 50 mL/min, and the pyrolytic vapors were further catalytically upgraded at 800 °C. TPR (Fig. S8) has shown that the iron oxide reduction peak is around 800 °C and the maximum temperature of microwave catalytic reaction is also about 800 °C. In order to verify the effect of catalyst reducibility on the catalytic performance, we evaluated the thermal pyrolysis-catalysis of LDPE using both fresh and the H_2-reduced (800 °C, 10%H_2/N_2, two hours) Fe-Co-Al catalysts. We have also conducted reduction at 500 °C and compared their performance to those reduced at 800 °C (Fig. S9). The results indicated that, although the catalyst reduced at lower temperature exhibited a higher hydrogen yield than 800 °C, its H_2 yield (around 46 mmol/g$_{plastic}$) was still significantly lower than that conducted under
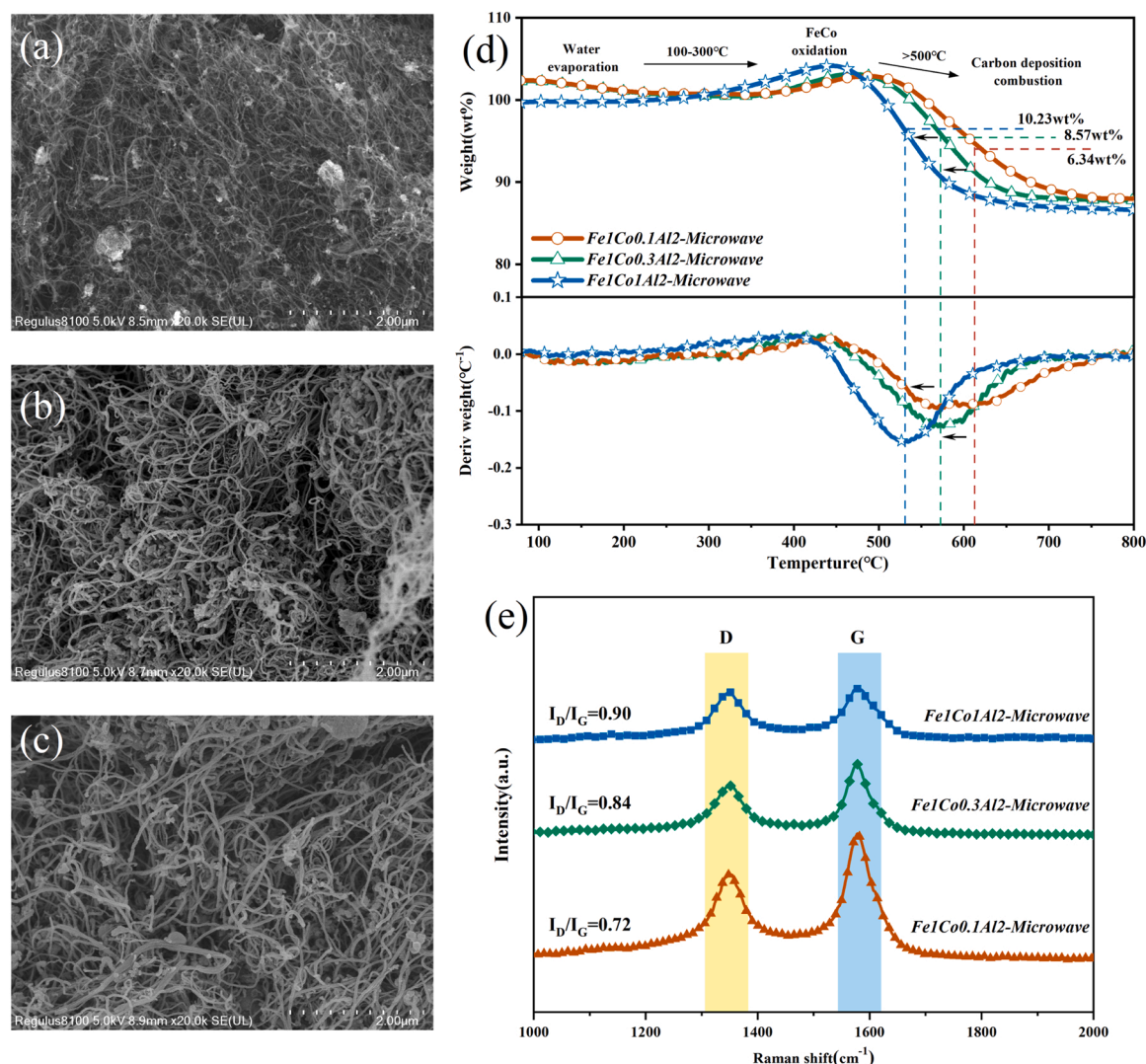
Fig. 8. FESEM images of spent (a) Fe1Co0.1Al2, (b) Fe1Co0.3Al2, and (c) Fe1Co1Al2 after microwave catalytic reaction, (d) Temperature programmed oxidation and (e) Raman analysis of carbon materials synthesized over Fe-Co-Al catalysts.

microwave field (61.39 mmol/g$_{plastic}$). As shown in Fig. 9a, traditional pyrolysis coupled with thermal catalysis using the same Fe-Co-Al catalysts showed a lower H$_2$ yield (maximum: 37.3 mmol/g$_{plastic}$) and H$_2$ concentration (maximum: 75.6 vol%) than microwave pyrolysis (Fig. 8d) in the gaseous products. In addition, a noticeable quantity of liquid products (2 wt% − 12 wt%) was obtained. The compounds detected in the liquid product are mostly polyaromatic hydrocarbons (Table S1 and S2), which are commonly considered as precursors of carbon deposits. It is also noteworthy that the traditional pyrolysis-catalysis process produced a much higher CH$_4$ content (up to 20 vol%) than microwave-initiated catalytic cracking. In the thermal catalytic cracking of polyethylene, methane is typically produced via sequential C-C bond scission and hydrogenolysis at high temperatures [51]. Consistent with microwave-initiated catalytic cracking, the positive role of Co on H$_2$ yield is also revealed in the case of the thermal pyrolysis-catalysis study. When the molar ratio of Co/Fe is increased from 0.1 to 1, the H$_2$ yield rises from 24.0 H$_2$/g$_{plastic}$ to 37.3 mmol H$_2$/g$_{plastic}$, while the volumetric concentration of H$_2$ rises from 57.5 vol% to 75.6 vol%. As discussed in the previous section, the phase transformation from ferrite spinel to FeCo alloy occurs rapidly during the reaction with microwave irradiation. This inspires us to examine the catalytic activity of the Fe-Co-Al catalyst in its reduced form. As expected, the H$_2$ yield (Fig. 9b) using the reduced catalysts

(10% H$_2$, 800 °C, two hours) increased to 34.02–40.04 mmol H$_2$/g$_{plastic}$ as compared to the unreduced ones, which validates the critical role of FeCo alloy formed via in situ reductions during catalytic cracking of LDPE.

The purity and graphitization degree of the carbon products from pyrolysis-catalytic cracking were investigated using TGA and Raman spectroscopy. The carbon deposits on the spent Fe-Co-Al catalysts from traditional pyrolysis-catalytic cracking exhibit higher I$_D$/I$_G$ than that from microwave-initiated catalysis, which implies a poorer graphic nature. In line with the microwave-initiated catalysis, I$_D$/I$_G$ shows a steady increasing trend with the increasing Co amount. Thermal carbon deposition (CNTs) (Fig. 9c) characterized by TG was measured to be 8.64%, 15.64%, and 15.89% for the Fe1Co0.1Al2, Fe1Co0.3Al2, and Fe1Co1Al2 catalysts at 800 °C respectively, which is consistent with the results trend in microwave performance. While as shown in Fig. 8d, the oxidation peak in DTG of microwave pyrolysis shows a slight reduction than thermal pyrolysis with the same Fe-Co-Al catalysts. This suggested that more filamentous carbon linked to the higher thermal stability of the carbon generated in thermal experiments. Besides, fewer amounts of carbon were deposited under microwave irradiation in Fig. 8d. This demonstrates that although the excessive Co in the catalysts could largely facilitate the generation of carbon nanotubes growth on metal sites, Fe-Co-Al catalysts were found to be difficult to deposit any carbons
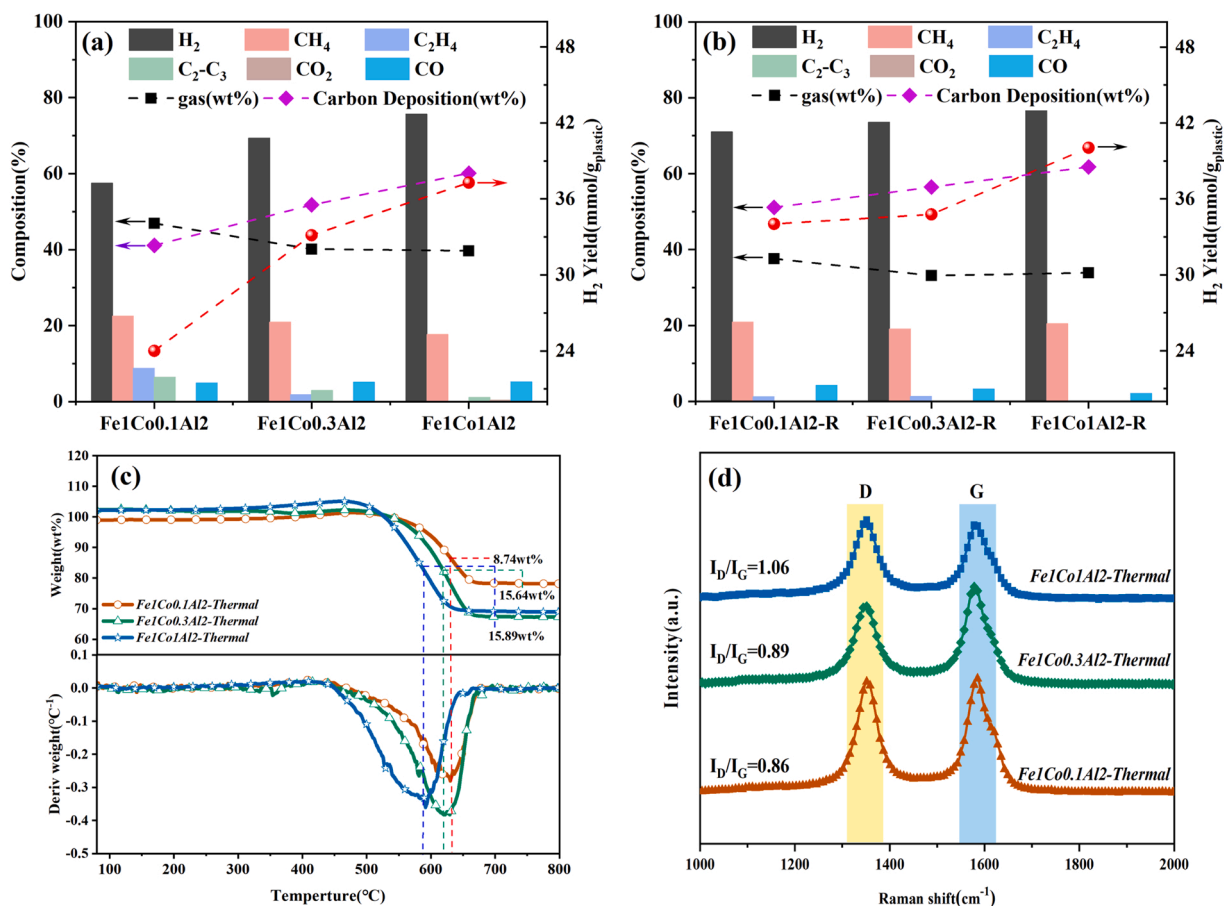
Fig. 9. Thermal experiments with (a) Fe-Co-Al catalysts, and (b) reduced Fe-Co-Al catalysts by H_2 (800 °C, two hours), (c) Temperature programmed oxidation, and (d)Raman analysis of carbon materials synthesized over Fe-Co-Al catalysts after thermal experiments.

due to metal agglomeration induced by microwaves. At the same time, thermal pyrolysis is likely to deposit more carbon materials, whereas the quality of the filamentous carbon is lower, with less ordered carbon walls than microwave catalysis, as observed by Raman. The comparative experimental study suggests that Fe-Co-Al catalysts can be readily reduced by microwave irradiation. The resulting highly reduced metal nanoparticles show high activity towards C-H bond cleavage. On the other hand, the low selectivity for C1-C4 hydrocarbons in microwave-initiated catalytic cracking suggests a relatively low C-C bond cleavage reaction rate. Due to these two effects, an exceptional H_2 yield is expected.

3.6. Effects of microwave irradiation on catalyst reduction through DFT calculation

In our study, a rapid formation of FeCo has been observed during microwave irradiation (Fig. 4), and consequently, a high hydrogen yield and low CO/CO_2 yield were acquired. The published studies also found that microwave irradiation shows a faster reduction of oxides than conventional heating [52,53].

Microwaves are electromagnetic waves coupled by an electric and a magnetic field orthogonal to each other with wavelengths of 1–1000 mm. Materials with permanent dipoles can be polarized via three different mechanisms, namely displacement polarization, orientation polarization, and interfacial polarization, by high-frequency electromagnetic fields. Such microwave-induced dipole polarization can accelerate the variation of phase composition and dielectric properties of the material being irradiated [54,55].

In addition, studies show that the electric fields can change the

electronic interactions, such as adsorption structures, vibrational frequencies, and oxidation states in catalysis system [56]. Jie et al. [9] also suggested the enhancement effect of the interfacial microwave electric field on the rapid desorption of H_2 from the catalyst surface.

On the basis of these findings, we inferred that microwave irradiation may affect the adsorption of reducing agent and the electronic interaction of reducing agent with oxides, which promotes the reduction of metal oxides. However, as the catalyst characterization tools that can be used under microwave fields are limited, it is hard to deeply understand the microwave field on the structural evolution of the studied catalyst. Therefore, density functional theory calculations were performed to calculate the change in adsorption energy and Bader charge under external fields. For simplicity, we did not consider the contribution of magnetic fields. Furthermore, previous studies have shown that microwave radiation is more conducive to breaking C-H bonds [14]. The C-H of light hydrocarbon is suggested to be activated via attacking of the electropositive H in the C-H bond by the nucleophilic surface oxygen of the catalysts, forming an O-H bond [57]. Meanwhile, due to the low yield of CO_2 and CO in the experiment indicated that reduction by carbon is not the primary metal reduction pathway. Thus, we assumed that hydrogen atom interaction with catalyst surface is the intermediate step in the microwave reaction process.

A $FeAl_2O_4$ (111) terrace was configured to represent the Fe-Al spinel catalyst. To investigate the hydrogen adsorption on $FeAl_2O_4$ (111) surface, we considered three possible adsorption sites, namely O1, O2, and Fe site (Fig. S10). The parameters of different adsorption configurations are listed in Table S4. O2 sites, i.e., the oxygen atom adjacent to Al, are the most favorable adsorption sites for H atoms, which exhibit the lowest adsorption energy of − 66.49 kJ/mol and the shortest O-H bond length

of 0.97 Å.

Then we analyzed the charge transfer and adsorption energy (E_{ad}) of the H atom under a varying electric field to shed light on the role of microwave irradiation. From table S5, the adsorption energy decreases along with the increase of the electric field applied in the positive Z direction, indicating that the positive electric field is not favorable for H adsorption. By contrast, E_{ad} increases from 0.7189 eV to 0.729 eV as the electric field intensity in the negative Z direction increases, suggesting that the negative electric field is favorable for H adsorption on the O2 sites of the FeAl$_2$O$_4$ (111) facet. This result suggested that microwave field might change the reduction of catalyst as well as adsorption and desorption energy of hydrogen on the surface of catalyst.

Fig. 10 and Fig. S11 show the Bader charge of surface Fe, H and Al atoms of a H-adsorbed and no H-adsorbed FeAl$_2$O$_4$(111) slab under the electric field with different intensities and directions. The Bader charge is assumed to agree with the oxidation state qualitatively. For the FeAl$_2$O$_4$(111) without H, the electric fields with different direction have opposite effect on the Bader charge of the surface Fe atoms. The surface Fe on the FeAl$_2$O$_4$(111) without absorbed H becomes more negative under positive electric fields, while it becomes more positive under negative electric fields. The dependence of charge transfer on field direction is probably attributed to the dipole moment of the asymmetric slab model system.

For the model of FeAl$_2$O$_4$(111) with adsorbed H, the application of electric fields decreased the number of electrons carried by the H atom under both positive and negative electric field. This suggested the electric field facilitated the electron flows from the H atom to FeAl$_2$O$_4$(111). Interestingly, although negative electric fields decrease the charge of the surface Fe on the FeAl$_2$O$_4$(111) without absorbed H atom (Fig. S11), either positive electric fields or negative electric fields (<-0.1 v/angstrom) increase the charge transfer on surface Fe atoms (atom number: 21–24) of FeAl$_2$O$_4$(111) with adsorbed H. This Bader charge analysis shows that the electric field will help change the oxidation state of the Fe in the presence of hydrogen.
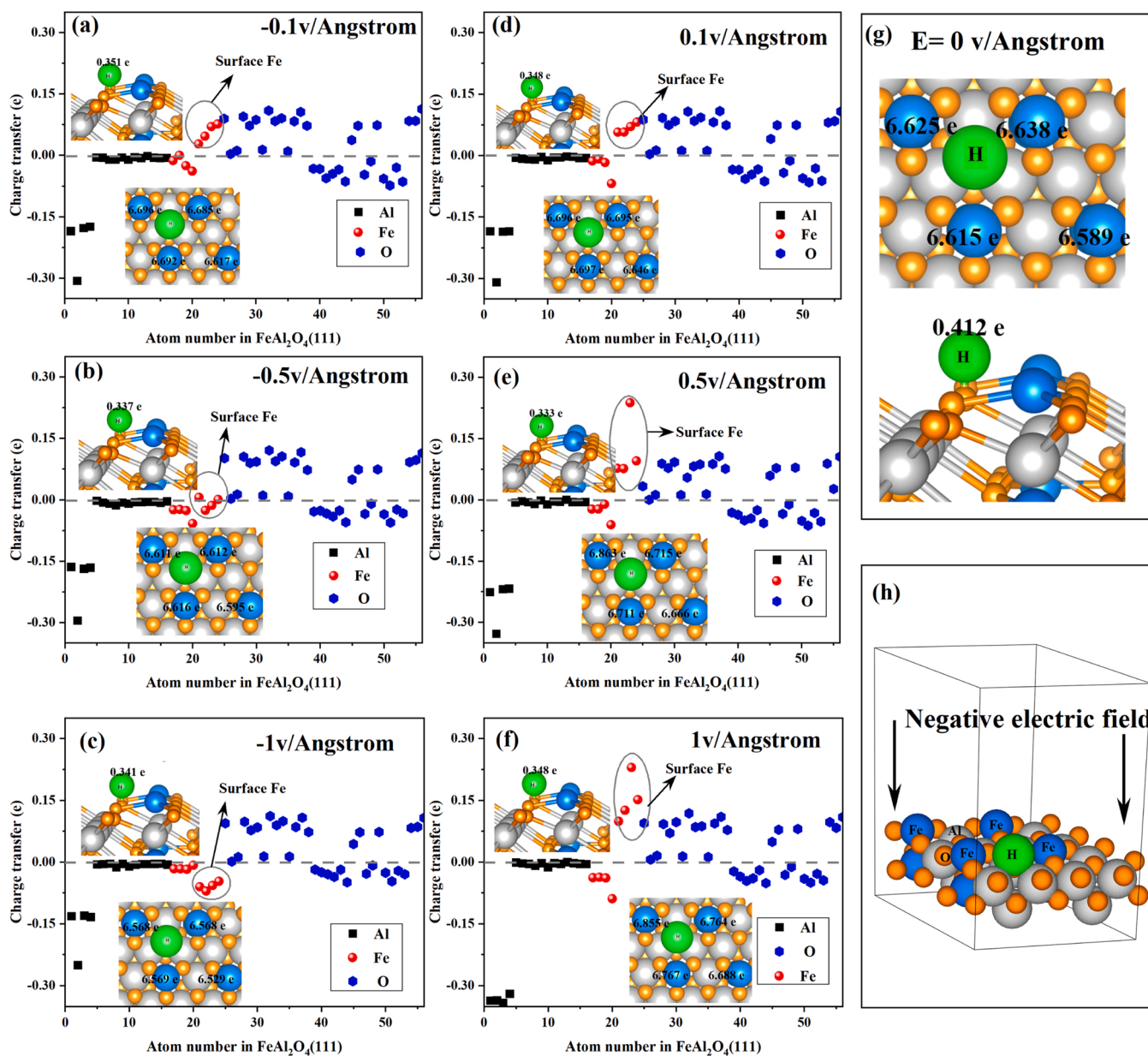
Fig. 10. (a-f) the Bader charge change of the Fe-Al slab model absorbing the H atom under different electric fields (Charge transfer = Bader charge under electric fields - Bader charge under no electric fields), (g) valence electrons distribution of H and surface Fe under no electric fields. (h) FeAl$_2$O$_4$(111) computational model under negative electric fields.

In a nutshell, we believe that the synergistic effect between microwave electric fields and catalysts promotes hydrogen production in several aspects. Firstly, it restricts the competing side reactions and enhances the C-H bond cleavage. The difference in dielectric properties caused by the compositional heterogeneity (e.g., active metals, catalyst support, defects, dopants) creates hotspots on the catalyst surface. The hot spots resulted in the depolymerization of LDPE on the contact interface of LDPE and the catalyst surface. The resulting hydrocarbon fragments are polarized on the catalyst's surface, and these polarized hydrocarbon fragments' C-H bonds are activated [14,58]. In addition, selective catalyst heating avoids overheating the whole catalyst bed, suppressing the undesired metal-catalyzed C-C bond breaking, which is commonly observed in conventional thermal catalysis. As a result, the increased hydrogen production rate is attributed to the increasing rate of C-H bond cleavage on activating catalysts and suppression of C-C bond cleavage.

Meanwhile, the microwave field affects the adsorption of hydrogen and the reduction of surface Fe species by the H atom. As a result, the fresh Fe-Al spinel was rapidly transferred to a highly dispersed metal catalyst supported on the aluminum oxide, which was believed to be a high-efficient chemical vapor decomposition catalyst.

4. Conclusion

In this study, spinel materials of Fe-Co-Al catalysts were prepared by a facile solution combustion method for microwave catalytic deconstruction of LDPE to produce hydrogen. The influence of Co-doped Fe-Al catalysts on microwave catalytic reactivity for plastic (LDPE) decomposition was evaluated. Specifically, we sought to understand the effects of microwave fields on the structural evolution of catalysts and hydrogen production. The main conclusions are:

(1) The Fe-Co-Al showed high hydrogen production activity (61.39 mmol/$g_{plastic}$,) for microwave-assisted plastic deconstruction. With an increase in Co doping, the hydrogen yield increased. Similarly, in the thermal catalytic decomposition of LDPE, the increase in Co doping also enhanced the H_2 yield.

(2) Besides increase in hydrogen yield, Co doping increases carbon yield but lowers the graphitization degree of carbon product in both microwave and thermal conversion. The rise in carbon yield and hydrogen yield is attributed to the fact that Co doping hinders the formation of Fe_3C, which changes the carbon diffusion pathway and promotes the formation of nanotubes and hydrogen.

(3) The microwave field has a significant effect on the transformation of iron oxides catalyst during reaction. Characterization indicated that the principal component of the fresh Fe-CO-Al catalysts is spinel $FeCoAlO_x$. During plastic decomposition, microwave field facilitates $FeCoAlO_x$ reduction, and the highly active phase, FeCo alloy, is rapidly formed. The DFT results indicated that the electric field in the microwave facilitated the reduction of the catalyst by enhancing the charge transfer from absorbed H to the metal. The DFT also indicated that electric field may affect the adsorption energy of H on iron catalyst, which is also an important fact that enhances the catalyst reduction and hydrogen production.

CRediT authorship contribution statement

Wentao Li: Methodology, Validation, Formal analysis, Writing – original draft, Writing – review & editing. **Kezhen Qian**: Writing – review & editing, Conceptualization, Methodology, Investigation, Formal analysis. **Zixu Yang**: Writing – review & editing, Methodology, Formal analysis. **Xiaoxu Ding**: Visualization, Validation. **Wenmin Tian**: Visualization, Validation. **Dezhen Chen**: Visualization, Validation.

Declaration of Competing Interest

The authors declare the following financial interests/personal relationships which may be considered as potential competing interests: Kezhen Qian reports financial support was provided by National Science Foundation. None.

Data Availability

Data will be made available on request.

Appendix A. Supporting information

Supplementary data associated with this article can be found in the online version at doi:10.1016/j.apcatb.2023.122451.

References

[1] R. Geyer, Chapter 2 - Production, use, and fate of synthetic polymers, in: T. M. Letcher (Ed.), Plastic Waste and Recycling, Academic Press, 2020, pp. 13–32.

[2] J.C. Acomb, C. Wu, P.T. Williams, The use of different metal catalysts for the simultaneous production of carbon nanotubes and hydrogen from pyrolysis of plastic feedstocks, Appl. Catal. B: Environ. 180 (2016) 497–510.

[3] R.-X. Yang, K.-H. Chuang, M.-Y. Wey, Effects of temperature and equivalence ratio on carbon nanotubes and hydrogen production from waste plastic gasification in fluidized bed, Energy fuels 32 (2018) 5462–5470.

[4] A.A. Aboul-Enein, A.E. Awadallah, Production of nanostructured carbon materials using Fe-Mo/MgO catalysts via mild catalytic pyrolysis of polyethylene waste, Chem. Eng. J. 354 (2018) 802–816.

[5] S.S. Sharma, V.S. Batra, Production of hydrogen and carbon nanotubes via catalytic thermo-chemical conversion of plastic waste, J. Chem. Technol. Biotechnol. 95 (2020) 11–19.

[6] D. Yao, Y. Zhang, P.T. Williams, H. Yang, H. Chen, Co-production of hydrogen and carbon nanotubes from real-world waste plastics: influence of catalyst composition and operational parameters, Appl. Catal. B: Environ. 221 (2018) 584–597.

[7] X. Liu, Y. Zhang, M.A. Nahil, P.T. Williams, C. Wu, Development of Ni-and Fe-based catalysts with different metal particle sizes for the production of carbon nanotubes and hydrogen from thermo-chemical conversion of waste plastics, J. Anal. Appl. Pyrolysis 125 (2017) 32–39.

[8] D. Yao, C. Wu, H. Yang, Y. Zhang, M.A. Nahil, Y. Chen, P.T. Williams, H. Chen, Co-production of hydrogen and carbon nanotubes from catalytic pyrolysis of waste plastics on Ni-Fe bimetallic catalyst, Energy Convers. Manag. 148 (2017) 692–700.

[9] X. Jie, W. Li, D. Slocombe, Y. Gao, I. Banerjee, S. Gonzalez-Cortes, B. Yao, H. AlMegren, S. Alshihri, J. Dilworth, Microwave-initiated catalytic deconstruction of plastic waste into hydrogen and high-value carbons, Nat. Catal. 3 (2020) 902–912.

[10] K.A. Shah, B.A. Tali, Synthesis of carbon nanotubes by catalytic chemical vapour deposition: a review on carbon sources, catalysts and substrates, Mater. Sci. Semicond. Process. 41 (2016) 67–82.

[11] H. Goyal, T.-Y. Chen, W. Chen, D.G. Vlachos, A review of microwave-assisted process intensified multiphase reactors, Chem. Eng. J. 430 (2022), 133183.

[12] Q. Wang, W. Xu, Z. Ma, F. Yu, Y. Chen, H. Liao, X. Wang, J. Zhou, Highly effective direct dehydrogenation of propane to propylene by microwave catalysis at low temperature over Co-Sn/NC microwave catalyst, ChemCatChem 13 (2021) 1009–1022.

[13] X. Bai, B. Robinson, C. Killmer, Y. Wang, L. Li, J. Hu, Microwave catalytic reactor for upgrading stranded shale gas to aromatics, Fuel 243 (2019) 485–492.

[14] X. Jie, S. Gonzalez-Cortes, T. Xiao, J. Wang, B. Yao, D.R. Slocombe, H.A. Al-Megren, J.R. Dilworth, J.M. Thomas, P.P. Edwards, Rapid production of high-purity hydrogen fuel through microwave-promoted deep catalytic dehydrogenation of liquid alkanes with abundant metals, Angew. Chem. Int. Ed. 56 (2017) 10170–10173.

[15] A. Ramirez, J.L. Hueso, R. Mallada, J. Santamaria, Microwave-activated structured reactors to maximize propylene selectivity in the oxidative dehydrogenation of propane, Chem. Eng. J. 393 (2020), 124764.

[16] S. Horikoshi, N. Serpone, Role of microwaves in heterogeneous catalytic systems, Catal. Sci. Technol. 4 (2014).

[17] H. Zhou, J.M. Saad, Q. Li, Y. Xu, Steam reforming of polystyrene at a low temperature for high H_2/CO gas with bimetallic Ni-Fe/ZrO_2 catalyst, Waste Manag. 104 (2020) 42–50.

[18] S. Zhang, S. Zhu, H. Zhang, X. Liu, Y. Xiong, High quality H$_2$-rich syngas production from pyrolysis-gasification of biomass and plastic wastes by Ni–Fe@ Nanofibers/Porous carbon catalyst, Int. J. Hydrog. Energy 44 (2019) 26193–26203.

[19] T. Hosoya, H. Kawamoto, S. Saka, Solid/liquid-and vapor-phase interactions between cellulose-and lignin-derived pyrolysis products, J. Anal. Appl. Pyrolysis 85 (2009) 237–246.

[20] L. Guo-Min, W. Lian-Cheng, X. Yao, Templated synthesis of highly ordered mesoporous cobalt ferrite and its microwave absorption properties, Chin. Phys. B 23 (2014), 088105.

[21] J.Y. Yusuf, H. Soleimani, Y. Noorhana, Y.K. Sanusi, L.L. Adebayo, S. Sikiru, F. A. Wahaab, Recent advances and prospect of cobalt based microwave absorbing materials, Ceram. Int. 46 (2020) 26466–26485.

[22] R. Ji, C. Cao, Z. Chen, H. Zhai, J. Bai, Solvothermal synthesis of Co$_x$Fe$_{3−x}$O$_4$ spheres and their microwave absorption properties, J. Mater. Chem. C 2 (2014) 5944–5953.

[23] D.A. Kutteri, I.-W. Wang, A. Samanta, L. Li, J. Hu, Methane decomposition to tip and base grown carbon nanotubes and CO$_x$-free H$_2$ over mono-and bimetallic 3d transition metal catalysts, Catal. Sci. Technol. 8 (2018) 858–869.

[24] V.D. Dasireddy, B. Likozar, Activation and decomposition of methane over cobalt-, copper-, and iron-based heterogeneous catalysts for CO$_x$-free hydrogen and multiwalled carbon nanotube production, Energy Technol. 5 (2017) 1344–1355.

[25] M. Pudukudy, Z. Yaakob, Z.S. Akmal, Direct decomposition of methane over SBA-15 supported Ni, Co and Fe based bimetallic catalysts, Appl. Surf. Sci. 330 (2015) 418–430.

[26] H.-Y. Mu, F.-T. Li, X.-T. An, R.-H. Liu, Y.-L. Li, X. Qian, Y.-Q. Hu, One-step synthesis, electronic structure, and photocatalytic activity of earth-abundant visible-light-driven FeAl$_2$O$_4$, Phys. Chem. Chem. Phys. 19 (2017) 9392–9401.

[27] M.-j Chai, X.-m Chen, Y. Zhao, R.-h Liu, J. Zhao, F.-t Li, Facile ionic liquid combustion synthesis and visible-light photocatalytic ability of mesoporous FeAl$_2$O$_4$ with high specific surface area, Chem. Lett. 43 (2014) 1743–1745.

[28] O.A. Bulavchenko, A.A. Pochtar', E.Y. Gerasimov, A.V. Fedorov, Y.A. Chesalov, A. A. Saraev, V.A. Yakovlev, V.V. Kaichev, Chemical and texture promoters in Cu-Fe-Al oxide nanocomposite catalysts for combustion of solid fuel gasification products, Appl. Catal. A: Gen. 590 (2020), 117364.

[29] M. Amoyal, R. Vidruk-Nehemya, M.V. Landau, M. Herskowitz, Effect of potassium on the active phases of Fe catalysts for carbon dioxide conversion to liquid fuels through hydrogenation, J. Catal. 348 (2017), 29-39-39.

[30] V. D'Ippolito, G.B. Andreozzi, D. Bersani, P.P. Lottici, Raman fingerprint of chromate, aluminate and ferrite spinels, J. Raman Spectrosc. 46 (2015) 1255–1264.

[31] S. Veena Kumari, V. Vaidyan, K. Sathyanarayana, Oxidation characteristics of artificially layered Fe/Al and Fe/Mg thin films, J. Mater. Sci. 27 (1992) 5504–5508.

[32] Z. Tong, Q. Yao, J. Deng, L. Cheng, T. Chuang, J. Wang, G. Rao, H. Zhou, Z. Wang, Effects of Ni-doping on microstructure, magnetic and microwave absorption properties of CoFe$_2$O$_4$, Mater. Sci. Eng.: B 268 (2021), 115092.

[33] M. Foerster, M. Iliev, N. Dix, X. Martí, M. Barchuk, F. Sánchez, J. Fontcuberta, The poisson ratio in CoFe$_2$O$_4$ spinel thin films, Adv. Funct. Mater. 22 (2012) 4344–4351.

[34] I. Jastrzębska, J. Szczerba, P. Stoch, A. Błachowski, K. Ruebenbauer, R. Prorok, E. Śnieżek, Crystal structure and mössbauer study of FeAl$_2$O$_4$, Nukleonika 60 (2015) 47–49.

[35] R. Stanfield, W. Delgass, Mössbauer spectroscopy of supported Fe-Co alloy catalysts for Fischer-Tropsch synthesis, J. Catal. 72 (1981) 37–50.

[36] C.T. Wirth, B.C. Bayer, A.D. Gamalski, S. Esconjauregui, R.S. Weatherup, C. Ducati, C. Baehtz, J. Robertson, S. Hofmann, The phase of iron catalyst nanoparticles during carbon nanotube growth, Chem. Mater. 24 (2012) 4633–4640.

[37] R. Yin, Fe-base alloys in CH$_4$/H$_2$ carburizing gas mixtures, Mater. High. Temp. 21 (2004) 205–211.

[38] X. Liu, J. Liu, Y. Yang, Y.-W. Li, X. Wen, Theoretical perspectives on the modulation of carbon on transition-metal catalysts for conversion of carbon-containing resources, ACS Catal. 11 (2021) 2156–2181.

[39] X.T. Tran, V.L.N. Vo, Y.-M. Chung, Fast microwave-assisted synthesis of iron–palladium catalysts supported on graphite for the direct synthesis of H$_2$O$_2$, Catal. Today (2022).

[40] A. Martínez de Yuso, J.-M. Le Meins, Y. Oumellal, V. Paul-Boncour, C. Zlotea, C. Matei Ghimbeu, Facile and rapid one-pot microwave-assisted synthesis of Pd-Ni magnetic nanoalloys confined in mesoporous carbons, J. Nanopart. Res. 18 (2016) 1–14.

[41] P. Kunal, T.J. Toops, A review of microwave-assisted synthesis-based approaches to reduce Pd-content in catalysts, Catalysts 10 (2020) 991.

[42] S. Wu, Y. Liu, Y. Ren, Q. Wei, Y. Sun, Microwave synthesis of single-phase nanoparticles made of multi-principal element alloys, Nano Res. 15 (2022) 4886–4892.

[43] M.C. Dimri, S.C. Kashyap, D. Dube, S. Mohanta, Complex permittivity and permeability of Co-substituted NiCuZn ferrite at rf and microwave frequencies, J. Electroceram. 16 (2006) 331–335.

[44] X. Xie, B. Wang, Y. Wang, C. Ni, X. Sun, W. Du, Spinel structured MFe$_2$O$_4$ (M=Fe, Co, Ni, Mn, Zn) and their composites for microwave absorption: A review, Chem. Eng. J. 428 (2022), 131160.

[45] M.A. Ermakova, D.Y. Ermakov, A.L. Chuvilin, G.G. Kuvshinov, Decomposition of methane over iron catalysts at the range of moderate temperatures: the influence of structure of the catalytic systems and the reaction conditions on the yield of carbon and morphology of carbon filaments, J. Catal. 201 (2001) 183–197.

[46] T. Hosoya, H. Kawamoto, S. Saka, Solid/liquid- and vapor-phase interactions between cellulose- and lignin-derived pyrolysis products, J. Anal. Appl. Pyrolysis 85 (2009) 237–246.

[47] Z. He, J.-L. Maurice, A. Gohier, C.S. Lee, D. Pribat, C.S. Cojocaru, Iron catalysts for the growth of carbon nanofibers: Fe, Fe$_3$C or both? Chem. Mater. 23 (2011) 5379–5387.

[48] M. Sveningsson, R.-E. Morjan, O. Nerushev, Y. Sato, J. Bäckström, E. Campbell, F. Rohmund, Raman spectroscopy and field-emission properties of CVD-grown carbon-nanotube films, Appl. Phys. A 73 (2001) 409–418.

[49] J.C. Acomb, C. Wu, P.T. Williams, Effect of growth temperature and feedstock: catalyst ratio on the production of carbon nanotubes and hydrogen from the pyrolysis of waste plastics, J. Anal. Appl. Pyrolysis 113 (2015) 231–238.

[50] N. Cai, S. Xia, X. Li, L. Sun, P. Bartocci, F. Fantozzi, H. Zhang, H. Chen, P. T. Williams, H. Yang, Influence of the ratio of Fe/Al$_2$O$_3$ on waste polypropylene pyrolysis for high value-added products, J. Clean. Prod. 315 (2021).

[51] T. Xie, G.R. Wittreich, D.G. Vlachos, Multiscale modeling of hydrogenolysis of ethane and propane on Ru(0001): Implications for plastics recycling, Appl. Catal. B: Environ. (2022), 121597.

[52] A. Amini, K.-i Ohno, T. Maeda, K. Kunitomo, Effect of the ratio of magnetite particle size to microwave penetration depth on reduction reaction behaviour by H$_2$, Sci. Rep. 8 (2018) 1–7.

[53] W.-H. Kim, S. Lee, S.-M. Kim, D.-J. Min, The retardation kinetics of magnetite reduction using H$_2$ and H$_2$-H$_2$O mixtures, Int. J. Hydrog. Energy 38 (2013) 4194–4200.

[54] Q. Yue, Z. Shao, S. Chang, J. Li, Adsorption of gas molecules on monolayer MoS$_2$ and effect of applied electric field, Nanoscale Res. Lett. 8 (2013) 1–7.

[55] J. Zhou, Z. You, W. Xu, Z. Su, Y. Qiu, L. Gao, C. Yin, L. Lan, Microwave irradiation directly excites semiconductor catalyst to produce electric current or electron-holes pairs, Sci. Rep. 9 (2019) 1–7.

[56] F. Che, J.T. Gray, S. Ha, N. Kruse, S.L. Scott, J.-S. McEwen, Elucidating the roles of electric fields in catalysis: a perspective, ACS Catal. 8 (2018) 5153–5174.

[57] Y. Wang, P. Hu, J. Yang, Y.-A. Zhu, D. Chen, C-H bond activation in light alkanes: a theoretical perspective, Chem. Soc. Rev. 50 (2021) 4299–4358.

[58] D. Balcells, E. Clot, O. Eisenstein, C-H bond activation in transition metal species from a computational perspective, Chem. Rev. 110 (2010) 749–823.